ADVANCED FUNCTIONAL MATERIALS
www.afm-journal.de

Room-Temperature Synthesis of High-Entropy Oxides via NH_4F Modulation for Dark •OH Radical-Enhanced Photothermal Catalysis

Yuerong Chen, Xiaowei Zhang, Tianhao Yan, Manchuan Guo, Jinliang Zhu, Ming Tang, Yanqiu Zhu, Zhangfa Tong, and Meiping Zhu**

High-entropy oxides (HEOs) are attracting extensive attention due to their flexible composition, tunable structures, and promising properties. However, their synthesis remains challenging, requiring high temperature, tedious steps, and expensive equipment. Herein, a room-temperature strategy is reported for synthesizing HEO as the dominant phase through a competitive complexation-precipitation equilibrium using NH_4F as a modulator. The resulting F-modulated HEO (HEO-F) tailored by NH_4^+ and F^- synergy, exhibits optimized lattice oxygen (O_{latt}), and oxygen vacancies (OVs) that significantly enhance the activation of reactants. Notably, HEO-F demonstrates superior capability for generating hydroxyl radicals (•OH) in the dark, which plays a critical role in promoting adsorption oxidation and sustaining catalytic stability. Under mild photothermal conditions ("light+120 °C"), it achieves complete toluene conversion with 100% CO_2 selectivity over 300 min and maintains long-term cyclic stability for more than 30 h. Detailed characterization and density functional theory (DFT) calculations are performed to link their properties to composition and structure. In situ diffuse reflectance infrared Fourier transform spectroscopy (DRIFTS) reveals that the key factors for facilitating deep oxidation and catalyst self-regeneration. This work demonstrates a simple, economicscopyal, and green room-temperature route for HEOs design and reveals the vital role of dark •OH for stable photothermal catalysis.

1. Introduction

Photothermal catalytic mineralization of refractory and toxic toluene into CO_2 and H_2O holds promise to tackle both air pollution and energy shortage. Solar-driven photothermal catalysis combines the advantages of photocatalysis and thermal catalysis, while overcoming their individual limitations, such as the low activity and stability for photocatalysis and the high energy consumption for thermal catalysis.[1,2] Mixed-valence oxides, such as Co_3O_4 and MnO_x, exhibit both photo-responsive property and thermal catalytic activity, good redox property and oxygen storage capacity, enabling them as efficient and cost-effective alternatives to noble metals.[3] However, their widespread practical photothermal catalytic application is hindered by their inevitable deactivation during long-term continuous operation, primarily due to the active site blockage and lack of oxygen species.[4]

Achieving complete mineralization of toluene via deep oxidation is crucial to mitigating catalyst deactivation. This process strongly depends on the abundance of reactive oxygen species (ROS) and mobile lattice oxygen. Among ROS, •OH radicals with a high redox potential (≈2.8 V vs RHE), play a crucial role in initiating radical chain reactions that mineralize toluene during photocatalysis.[5,6] Meanwhile, enhanced lattice oxygen (O_{latt}) mobility in Mn-based oxides has been shown to be essential for promoting the deep removal of toluene in thermal catalysis.[7] Oxygen vacancies (OVs) engineering has been widely recognized as a pivotal strategy for enhancing the photothermal catalytic performance. OVs can serve as critical active sites that facilitate electron transfer and modulate redox properties, thereby promoting the generation, subsurface storage, and diffusion of ROS.[8] In addition, OVs can function as Lewis acid sites that enhance adsorption and activation of reactants (e.g., O_2, H_2O, and toluene), while simultaneously improving lattice oxygen mobility.[9] Unlike common element doping that was constrained by low solubility limits, Zhang et al. proposed the configurational entropy engineering as a superior strategy for effective tuning of OVs.[10] High-entropy engineering of oxides, enabled by five or more principal elements incorporating into a single-phase solid solution structure, have recently garnered increasing interest in catalytic applications, as their resulting pronounced lattice distortion that could effectively promote lattice

Y. Chen, X. Zhang, T. Yan, M. Guo, J. Zhu, M. Tang, Y. Zhu, M. Zhu
School of Resources
Environment and Materials
Guangxi Key Laboratory of Processing for Non-ferrous Metals and Featured Materials
Guangxi University
Nanning 530004, P. R. China
E-mail: jlzhu@gxu.edu.cn; meipingzhu@gxu.edu.cn
Z. Tong, M. Zhu
Guangxi Key Laboratory of Petrochemical Resource Processing and Process Intensification Technology
Guangxi University
Nanning 530004, P. R. China
The ORCID identification number(s) for the author(s) of this article can be found under https://doi.org/10.1002/adfm.202526117

DOI: 10.1002/adfm.202526117

oxygen activation.[11] Particularly, the flexible composition and unique structure of high-entropy engineering oxides enable tailored electronic and band structures, which provide great flexibility for optimizing photothermal performance.[12] Nevertheless, since the pioneering report of entropy-stabilized oxides by Rost et al. in 2015,[13] the synthesis of high-entropy engineering oxides largely relies on conventional high-temperature routes (>900 °C), suffering from several limitations, such as high energy demands, expensive equipment requirements, and poor catalytic performance due to low specific surface area and limited active site accessibility.[14]

Low-temperature synthesis routes for high-entropy engineering oxides have attracted growing interest for their potential to overcome these drawbacks. However, most current methods, such as microwave-assisted solvothermal,[15] sol-gel electrospinning,[16] solution combustion,[17] and liquid metal-induced hydrothermal,[18] still require elevated temperatures (typically above 200 °C), and are hampered by issues such as complex procedures, specialized equipment, safety risks like fire and explosion, or high material and operational costs. Very recently, a novel class of rare-earth high-entropy compounds (carbonates/hydroxycarbonates) has been reported to be obtainable through co-precipitation and hydrothermal treatment at relatively lower temperatures (140 °C).[19] However, this route resulted in the formation of carbonate/hydroxycarbonate phases, which are distinct from the desired oxide phases. Notably, an ultrasound-mediated co-precipitation method reported by Siniard et al. could directly obtain high-entropy engineering oxides (e.g., $CuCoFeNiMnO_x$) under ambient conditions. This strategy resulted nanocatalysts exhibited high surface area and abundant OVs driven by cavitation-induced nucleation.[20] Inspired by this principle of controlling nucleation kinetics via external stimulation, we hypothesized that a more versatile chemical strategy could be devised. We propose that a competitive dissolution-precipitation process, coupled with strongly oxidizing anionic modulation during nucleation and growth, could provide superior control over precursor kinetics and oxide phase formation.

Herein, we report a room-temperature synthesis of a MnCo-based high-entropy oxide with fluorine doping (HEO-F) via an NH_4F-medulated route, which was driven by a competitive complexation-precipitation equilibrium. The synthesis was conducted under alkaline conditions similar to those for MnCo-based high-entropy layered double hydroxide (HELH), which served as a key mechanistic counterpart to highlight the distinct role of NH_4F in redirecting oxide phase transformation for photothermal catalysis. Control experiments were conducted to reveal the key factors driving the formation of oxide phase and the "competitive complexation-precipitation equilibrium" mechanism for HEO-F synthesis. Systematic characterizations verify the morphology and structural evolution of HEO-F compared to those of HELH. In addition, DFT calculations based on the active phases indicate the enhanced adsorption and activation toward reactants. Particularly, the key role of dark •OH radical-enhanced photothermal catalysis is verified by control experiments for radical generation and trapping. Photothermal catalytic tests demonstrate that the HEO-F catalyst exhibits exceptional photothermal catalytic activity, selectivity and good stability for toluene mineralization. Furthermore, in situ DRIFTS analysis was performed to reveal the toluene conversion pathway and photothermal synergistic mechanism. Long-term cyclic tests demonstrate the excellent regeneration ability of HEO-F. This study provides a facile and mild synthesis route for HEOs that enables efficient and stable photothermal catalysis in long-term continuous operation.

2. Results and Discussion

2.1. Preparation and Characterization of Catalysts

Figure 1a depicts the schematic for preparing crystalline HELH and amorphous halogen-modulated HEO-X (X = Cl/F). Different from the HELH prepared by the traditional co-precipitation method, the novel HEOs were synthesized through a competitive complexation-precipitation strategy. First, NH_4X (X = Cl/F) was dissolved in a mixed M^{2+}/M^{3+} solution (Solution A). The substantial molar excess of X^- anions over cations (X^-: (M^{2+}/M^{3+}) ≈ 9:1) promoted the formation of primary $[M(X)_6]^{2+/3+}$ coordination spheres, while excess X^- and NH_4^+ established secondary hydrogen-bonded spheres according to coordination chemistry. The Solution A then dropwise added to 25 mL alkaline solution (Solution B, pH 10), in which the X^- ligands of $[M(X)_6]^{2+/3+}$ were completely displaced by the OH^- to form $[M(OH)_m]^{2+/3+}$ hydroxide nuclei, while the NH_4^+ consumed OH^- to form NH_3 and H^+ until $[NH_3] \approx [OH^-]$. Next, in situ generated NH_3 competitively displaced OH^- ligands from kinetically labile cations in the primary spheres and formed $[M(NH_3)_6]^{2+/3+}$, due to its stronger field ligand than OH^- according the crystal field theory. This disruption of layered nucleation was counterbalanced by outer OH^- anions with stably higher concentrations (initial pH maintained at 10 via additional NaOH), establishing a dynamic complexation-precipitation equilibrium ($M(OH)_m$ (s) + $nNH_3 \leftrightarrow M(NH_3)_n^{m+}$ + mOH^-).[21]

The direction of the complexation-precipitation equilibrium could be controllable through modulating initial pH and the addition of additives that disrupt the nucleation. After mixing Solution A and B, maintaining the initial pH stable at 10 required 7, 37, 28, and 41 mL of NaOH (3 M) for HELH, HEO-Cl, HEO-F, and HEO-F-pH12, respectively (Table S1, Supporting Information). The pH difference (ΔpH) after 48 h was 0.19, 0.03, and 0.1 for HELH, HEO-Cl, and HEO-F (Figure S1, Supporting Information). The highest NaOH demand with near-zero ΔpH for HEO-Cl signifies rapid dissolution-precipitation equilibrium. In contrast, clearly lower NaOH consumption but sustained ΔpH for HEO-F reflects slow $[M(NH_3)_n]^{m+}$ dissociation enabling steady reconstruction. Notably, the inverse change trend of NaOH consumption between HEO-F and HEO-F-pH12 relative to HEO-Cl suggests that high pH suppresses NH_3 complexation ($M(NH_3)_n^{m+}$ + mOH^- → $M(OH)_m$ (s) + nNH_3), forcing excessive base addition. The resulting metastable metal coordination networks facilitate amorphous HEO growth under ambient conditions. Meanwhile, surface X^- anions tend to partiasubstituteuted lattice oxygen due to higher M-X bonding energy (X = F/Cl), modulating surface energy to direct morphology evolution.[22]

The morphology, elemental and structural characteristics of HELH, HEO-Cl, and HEO-F were analyzed by SEM, EDS, and TEM, respectively. As shown in Figure S2 (Supporting Information), pristine HELH displays micron-scale agglomerates of

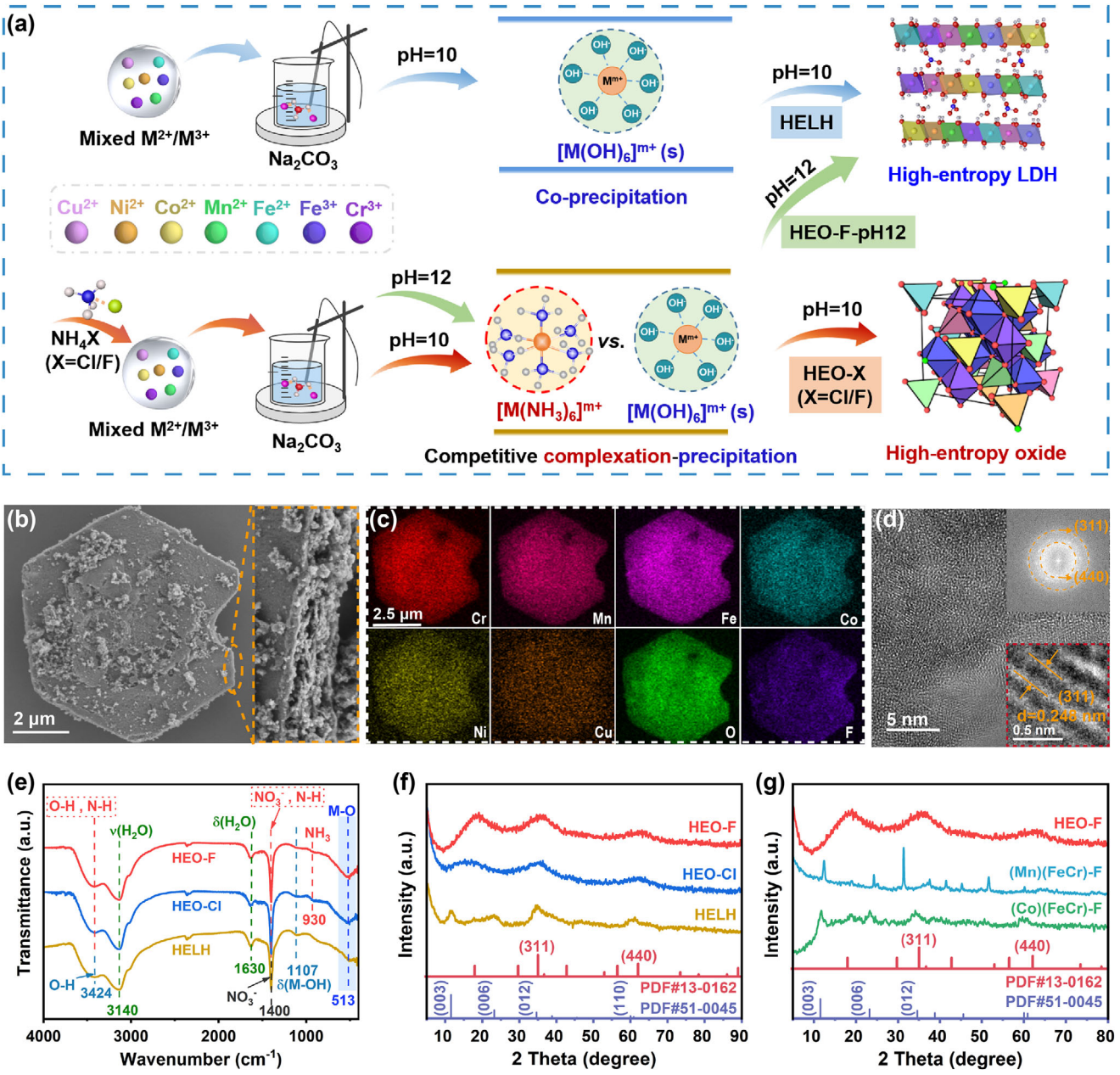

Figure 1. a) Schematic of the synthesis process for high-entropy materials; b) SEM images and c) EDS mapping images of HEO-F; d) HR-TEM image, lattice spacing (bottom right) and SAED (upper right) under the fast Fourier transform (FFT) of HEO-F; e) FT-IR spectra and f) XRD patterns of HELH, HEO-Cl and HEO-F; g) XRD patterns of (Co)(FeCr)-F, (Mn)(FeCr)-F, and HEO-F.

stacked lamellar sheets, with a rough surface sparsely decorated by submicron particles. EDS elemental mapping analysis confirms the homogeneous distribution of Cr, Mn, Fe, Co, Ni, Cu, and O element. By comparison, HEO-Cl exhibits micron-scale aggregates consisting of regularly and loosely stacked sub-micron layers, and contains all elements similar to HELH with additional Cl element that are uniformly distributed on the surface (Figure S3, Supporting Information). TEM result (Figure S4, Supporting Information) reveals that HEO-Cl aggregates with interconnected submicron sheets. The uniformly and significantly reduced layered size is possibly due to rapid disruption of layered nucleation induced by the NH_4^+ and Cl^- synergy. In contrast, Figure 1b and Figure S5 (Supporting Information) reveal that HEO-F forms hollow layered hexagonal plates with micron-scale lateral size and submicron thickness. Sparse particles exist on its distinct disrupted surface and within interlayers, which is possibly due to the effect of complexation-dissolution and reconstruction. This surface disruption vanishes in HEO-F-pH12 (prepared at pH12), suggesting that optimal pH is key for the occurrence of complexation-dissolution (Figure S6, Supporting Information). All elements similar to HEO-Cl, with Cl replaced by F dopant, are homogeneously distributed on HEO-F and

HEO-F-pH12 surfaces, as revealed by EDS element mapping analysis in Figure 1c and Figure S7 (Supporting Information), respectively. TEM image (Figure S8, Supporting Information) further confirms the hollow platelet architecture of HEO-F, with observed irregular nanosized fragments. Furthermore, HELH-NaF (obtained by replacing the NH_4F with NaF) also displays a 2D morphology (mixed thin nanosheets with significantly reduced thickness) (Figure S9, Supporting Information). These observations demonstrate the synergistic NH_3 complexation and F^- modulation enables slow $[M(NH_3)_n]^{m+}$ dissociation, driving steady reconstruction to form unique hollow layered platelet architecture of HEO-F. Contrasting sharply with the particulate aggregates of HEO-Cl further indicates that F^- modulation induces lateral layered structures at room temperature, while the thickness regulation and size refinement are controlled by the NH_4^+ addition.

The metal ratios of the as-prepared materials were determined by SEM-EDS, and ICP-AES, and the results are displayed in Figure S10 (Supporting Information) (detailed in Tables S2 and S3, Supporting Information). Both techniques confirm that HELH exhibits a molar ratio close to 1:2:1:1:1:1 for Mn, Fe, Co, Ni, Cu, and Cr. Given the equimolar addition of Fe_{II} and Fe_{III} precursors, this corresponds to A-site divalent cations (Mn, Fe_{II}, Co, Ni and Cu) at ≈1:1:1:1:1 and B-site trivalent cations (Fe_{III} and Cr) at ≈1:1, which is consistent with the addition ratios. The configuration entropy of HELH was calculated to be 1.94 R based on the ICP-ACS data (Table S3, Supporting Information), indicating its high-entropy state and equimolar cation distribution. In contrast, both HEO-Cl and HEO-F show significant deviation from equimolar A-site incorporation, manifested by sequentially decreasing Co, Ni, and Cu ratios below the equimolar average, while Fe and Mn ratios increase above the equimolar average (Figure S10, Supporting Information). This non-equimolar A-site distribution originates from the competition between M-NH_3 complexation (dissolution) and M-OH precipitation during synthesis. The reduced incorporation of Co^{2+}, Ni^{2+}, and Cu^{2+} is attributed to their tendency to form more stable $[M(NH_3)_n]^{2+}$ complexes (preferential dissolution), as dictated by the $[M(NH_3)_n]^{2+}$ stability order: $Mn^{2+} < Fe^{2+} < Co^{2+} < Ni^{2+} < Cu^{2+}$.[23] Despite this non-equimolar A-site distribution, the configuration entropies of HEO-Cl and HEO-F were calculated to be 1.81 and 1.77 R, respectively, reflecting that HEO-Cl and HEO-F remain within the high-entropy regime. In addition, it is noteworthy that HEO-F-pH12 maintains near-equimolar cation distribution (EDS, Table S2, Supporting Information), which is directly contrasting with HEO-F. The opposite result is consistent with NaOH consumption trend as described above, indicating that the pH is the critical factor governing the M-NH_3/M-OH competition equilibrium. Thus, HEO-X (X = Cl/F) materials in a high-entropy state were successfully fabricated through a competitive complexation-precipitation strategy, with A-site cation distributions (equimolar or non-equimolar) controllably mediated by pH and competitive complexation.

FTIR spectroscopy was performed to determine surface functional groups of the as-prepared samples (Figure 1e). HELH displays a typical hydroxide spectrum, where a broad band at 3424 cm^{-1} is due to the stretching vibration of -OH groups (ν(O-H)),[24] two peaks at 3140 and 1630 cm^{-1} are individually ascribed to the stretching vibration and bending vibration of interlayer H_2O,[25] a sharp and strong IR peak observed at 1400 cm^{-1} corresponds to the vibration of intercalated ions (NO_3^-), and two weak bands at 1107 and 513 cm^{-1} are attributed to the bending vibration of M-OH and M-O (δ(M-OH) and δ(M-O)),[24,25] respectively. HEO-Cl and HEO-F inherit all the IR bands of HELH, in addition to a new weak peak at 930 cm^{-1} caused by the vibration of NH_3.[26] There are almost no changes in the FTIR spectra of two NH_4^+ added samples (HEO-Cl and HEO-F). However, obvious differences can be observed when compared to pure HELH. This distinct difference suggests that the NH_4^+ ions plays a dominant role in influencing the coordination environment, while the effects of F^- and Cl^- ions are negligible. Specially, when compared with the FTIR spectrum of HELH, the peaks at 3424 and 1400 cm^{-1} for HEO-Cl and HEO-F are found to become stronger due to combinational N-H vibrations,[27] which are in good agreement with the emerged NH_3 peak. Besides, the intensity of δ(M-OH) peak is diminished, while that of δ(M-O) peak is clearly intensified, which suggests that the transformation of M-OH into M—O bond in the lattice.

The crystalline structure and phase composition of the as-formed materials were further characterized by HRTEM and XRD. The HRTEM image of HELH (Figure S11, Supporting Information) shows distinct lattice fringes with a spacing of 0.259 nm, corresponding to the (012) plane. Its polycrystalline nature is confirmed by clear selected area electron diffraction (SAED), which also reveals diffraction rings indexed to (012), (015), and (110) planes. This is further confirmed by the XRD result that HELH displays diffraction peaks at 11.5, 23.2, 34.6, and 60° indexed to (003), (006), (012), and (110) planes of hydroxide, respectively (Figure 1f). In contrast, both HEO-Cl and HEO-F (Figure S12, Supporting Information; Figure 1d) exhibit an amorphous matrix lacking discernible lattice fringes, with sparsely embedded nanocrystalline domains (<5 nm). These domains show lattice fringes indexed to (311) plane, while their SAED patterns display diffuse rings assignable to (311) and (440) planes, confirming successful construction of amorphous-crystalline nanocomposites via M-NH_3 complexation competition. Figure 1f displays that those obvious diffraction peaks of hydroxide phase are disappeared in the XRD patterns of HEO-Cl and HEO-F, and the two broader and weaker peaks attributed to (311) and (440) planes further verify the oxide phase with amorphous-crystalline characteristics. This result is consistent with the transformation of M-OH into M-O as revealed by FTIR analysis. The thermogravimetric analysis in air (Figure S13, Supporting Information) shows that the weight loss related to the lattice hydroxyl groups within 170–400 °C is much lower in HEO-F than that in the hydroxide counterpart (HELH),[28] indicating a substantial reduction in hydroxyl group content due to the phase transformation.

To further clarify the roles of NH_4^+ and F^-, Figure S14a (Supporting Information) shows the XRD patterns for samples prepared with NaF, NH_4Cl, and NH_4F, exhibiting diffraction patterns consistent with hydroxide (PDF#51-0045) and oxide (PDF#13-0162), respectively. These comparisons clearly demonstrate the key role of NH_4^+ in the formation of oxide phase. Notably, the diffraction peaks of the NH_4Cl and NH_4F are significantly broader than those with NaF-derived sample, revealing their partial amorphous structure. This amorphous structure of NH_4^+-containing sample promotes the formation of OVs

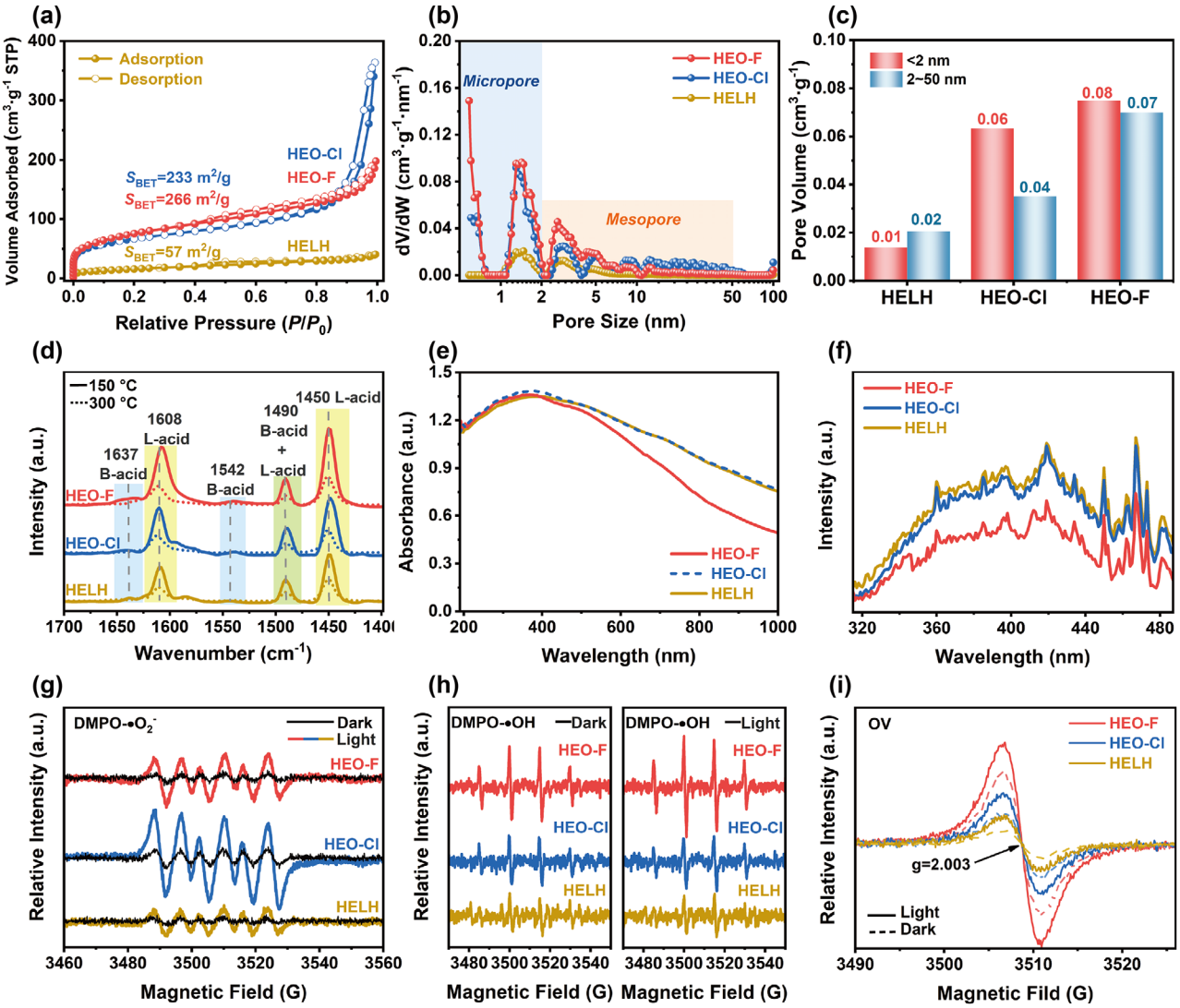

Figure 2. a) N_2 adsorption-desorption isotherms, b) pore diameter distribution curves, c) pore volume, d) Py-IR spectra obtained at 150 and 300 °C, e) UV-vis diffuse reflectance spectroscopy, and f) photoluminescence emission spectra (under excitation at λ = 250 nm) of HELH, HEO-Cl, and HEO-F; EPR spectra of g) DMPO-•O_2^-, h) DMPO-•OH, and i) oxygen vacancies of HELH, HEO-Cl, and HEO-F in the dark and after exposure to the light for 10 min.

accompanying with the F^- modulation, as revealed by a significantly stronger EPR peak at g = 2.003 in HEO-F relative to that in HEO-Cl (**Figure 2i**). These results illustrate that the vacancy generation is driven by the synergistic effect of NH_4^+ and F^-, while the oxide phase formation was primary dependent on the NH_4^+. Furthermore, Figure S14b (Supporting Information) displays the pH-dependent phase evolution using a similar addition of NH_4^+ (i.e., by varying the NH_4^+/OH^- ratio). The diffraction patterns of the samples obtained at pH12, pH11, and pH10 are indexed to hydroxide (PDF#51-0045), a mixed hydroxide-oxide intermediate, and oxide (PDF#13-0162), respectively. The presence of a distinct intermediate phase at pH11 confirms the proposed "competitive complexation-precipitation equilibrium". This suggests the gradual phase transition is governed by the interplay between NH_4^+-induced NH_3 complexation and OH^--induced co-precipitation kinetics of the mixed metal ions.

Combined with the above characterizations, it confirms that the direction of complexation-precipitation equilibrium influenced by the NH_4^+/OH^- ratio profoundly impacts the formed phase structure. During the competitive complexation-precipitation, multiple mixed metal ions serve as another critical factor influencing oxide formation. As shown by the XRD results (Figure 1g), the HEO-F sample with multiple metal ions in A-site exhibits oxide phase, while (Mn)(FeCr)-F and (Co)(FeCr)-F samples with single metal ions in A-site show distinct hydrotalcite peaks, indicating that the formation of oxides via complexation-precipitation is facilitated by high-entropy mixed condition. Therefore, there are both the NH_4^+/OH^- ratio and multiple mixed metal ions that collectively affect the oxide phase formation. This strategy provides a simpler, more economical and greener route for HEOs fabrication compared to other low-temperature synthesis methods (Table S4,

Supporting Information), which is promising for scalable industrial applications.

To further probe the surface chemical compositions and their valence states, XPS spectra of HELH, HEO-Cl, and HEO-F were analyzed and are shown in Figure S15 (Supporting Information). The survey spectra (Figure S15a, Supporting Information) confirm the presence of Cr, Mn, Fe, Co, Ni, Cu, and O in all samples, consistent with ICP-AES results. The detailed peak positions and assignments from the deconvoluted high-resolution XPS spectra are summarized in Table S5 (Supporting Information).[29–31] High-resolution spectra (Figure S15b–g, Supporting Information) reveal that Cr is present as Cr^{3+}, while Mn, Fe, Co and Ni exist in mixed +2 and +3 states. Cu is only detected in HELH. Compared to HELH, the Cr^{3+} ($2p_{3/2}$) peak position remains almost unchanged in HEO-Cl and HEO-F. Notably, the Mn^{2+}/Mn^{3+} ($2p_{3/2}$) peaks of HEO-Cl and HEO-F exhibit apparent positive shifts relative to those of HELH, with slightly larger shift in HEO-Cl versus HEO-F, indicating that NH_3 complexation induces a distinct electron-deficient state at Mn sites. Similarly, a minor positive shift in the Fe^{2+}/Fe^{3+} ($2p_{3/2}$) peaks is observed in both HEO-Cl and HEO-F compared to HELH. Furthermore, the Co $2p_{3/2}$ peaks of HEO-Cl and HEO-F shift to higher binding energies than those of HELH, confirming an enhanced electron-deficient state. Notably, this effect is much stronger with F^- than Cl^- modulation, which contrasts with the trend observed at the Mn sites. In addition, the Ni^{2+} ($2p_{3/2}$) peaks of both HEO-Cl and HEO-F exhibit an obvious negative shift, suggesting electron accumulation at Ni sites caused by NH_3 complexation. This behavior is apparently opposite to that of Mn and Co, suggest internal electron transfer among the multi-metal sites.

These results demonstrate that the synergistic strategy of NH_3 complexation and halide modulation selectively tunes the electronic interaction between Mn, Co, and Ni, resulting in significantly enhanced oxidizing capability of the key active sites (Mn and Co) for photothermal oxidation. More importantly, oxygen species analysis (Figure S15h,i, Supporting Information) shows increased lattice oxygen (O_{latt}/O_{all}) and decreased hydroxyl oxygen (O_{OH}/O_{all}) from HELH to HEO-Cl/HEO-F, further evidencing the room-temperature oxidation induced by NH_3 complexation, promoting phase transformation from hydroxide to oxide. Notably, HEO-F exhibits higher adsorbed oxygen (O_{ads}/O_{all} = 57%) than HEO-Cl (52%) or HELH (49%), highlighting the role of F^- modulation is critical for increasing O_{ads}. These results collectively demonstrate the synergistic regulation of NH_4^+ and X^- (X = F/Cl) for optimizing electronic structure and oxygen species, which is critical for enhancing Lewis acidity and promoting photothermal catalytic toluene conversion.

2.2. Adsorption, Photoelectric, Photothermal Properties, and ROS Generation

N_2 adsorption-desorption isotherms were performed to determine the surface area and pore size distribution of all three samples, and the results are shown in Figure 2a,b, respectively. As displayed in Figure 2a, HELH exhibits a type I adsorption isotherm with extremely low N_2 uptake, suggesting that it has a small specific surface area and poor porosity. In contrast, significently higher N_2 uptakes are observed in both NH_3-complexed samples (HEO-Cl and HEO-F), implaying that NH_3 complexation promotes pore formation and increase of specific surface area. Specifically, they display similar type IV adsorption isotherms, with HEO-F exhibiting a slightly higher adsorption capacity. In addition, H3-type and H4-type hysteresis loops in the P/P_0 ranges of 0.8–1.0 and 0.5–1.0 are occured in HEO-Cl and HEO-F, respectively, implying the presentence of tapered meso-/macropores[32] and interconnected slit-shaped micropores/mesopores.[33] For quantitative evaluation, the Brunauer-Emmett-Teller (BET) specific surface area (S_{BET}) was further calculated and the S_{BET} values follow the order: HELH (57 $m^2 g^{-1}$) < HEO-Cl (233 $m^2 g^{-1}$) < HEO-F (263 $m^2 g^{-1}$), which is consistent with the N_2 adsorption trends. It is noteworthy that the S_{BET} of the NH_3-complexed samples (HEO-Cl and HEO-F) is 3.1–3.6 times higher than that of HELH, with F-modified sample showing the highest value.

Figure 2b shows the pore size distributions obtained using DFT model. HELH exhibits two weak peaks in the micropore and mesopore regions, located at 1–2 and 2–5 nm, respectively. In contrast, both HEO-Cl and HEO-F exhibit notably stronger peaks in these ranges, along with a notable new sub-1 nm (ultramicropore) distribution. Given the kinetics diameter of the reactants (O_2, H_2O, and toluene) <1 nm, pore volumes for primary adsorption pores (<2 nm) and diffusion-channel pores (2–50 nm) were estimated and are displayed in Figure 2c. Both pore volumes exhibit the identical sequence: HELH < HEO-Cl < HEO-F, with values increasing from 0.01 to 0.06 and 0.08 $cm^3 g^{-1}$ (adsorption), and 0.02 to 0.04 and 0.07 $cm^3 g^{-1}$ (diffusion). These results reveal the NH_3 complexation collaboratively with Cl^-/F^- modulation during high-entropy synthesis enhances both micropore and mesopore porosity. Therein, the hollow layered hexagonal plate morphology furthter promotes HEO-F to obtain the largest specific surface area and highest pore volumes, which is beneficial for facilitating toluene adsorption and diffusion.

In addition, the reactant adsorption and activation are highly dependent on the surface acidity of catalysts. Py-IR spectra collected at 150 and 300 °C were employed to distinguish total and strong acid sites, respectively. As illustrated in Figure 2d, all three samples in both spectra exhibit three distinct peaks (1450, 1490, and 1608 cm^{-1}) and two negligible peaks (1542 and 1637 cm^{-1}), which correspond to pyridine chemisorbed on Lewis (L) and Brønsted (B) acid sites, respectively, with the 1490 cm^{-1} peak indicating both L and B sites.[34] This indicates that the surface acidity of the three catalysts is mainly dominated by L-acid sites. The total concentration of L-acid sites (150 °C) of HELH, HEO-Cl, and HEO-F was quantified and determined to be 27.36, 40.82, and 49.59 μmol g^{-1}, respectively (Table S6, Supporting Information). A similar trend is also observed in the concentration of strong L-acid sites (300 °C). The significant increase in both total and strong Lewis acidity for HEO-F highlights the advantages of the NH_3 complexation and F^- modulation synergy: 1) NH_3 complexation can obviously enhance the Lewis acidity by disrupting the coordination environment during HEO-F formation; 2) The higher electronegativity of the F^- ions (Pauling: 3.98 vs Cl^-: 3.16) further intensifies the Charge redistribution at unsaturated metal sites (Mn and Co) and the formation of oxygen vacancies (OVs),[35,36] as evidenced by the XPS and EPR results above. Given the Lewis basic properties of the key reactants including O_2, H_2O and toluene, NH_4^+-F^- pairs enhance the

Lewis acidity in HEO-F, promoting the catalyst-reactant (Lewis acid-base) interactions.[37] Specifically, this results in an obviously higher toluene desorption temperature for HEO-F than that for HELH, due to enhanced chemical adsorption, as shown by the toluene-TPD results (Figure S16, Supporting Information). This is favorable for promoting the toluene adsorption and activation (especially for the C—H bond dissociation).[37]

Following the reactant adsorption, photon absorption by the catalyst will generates electron-hole pairs to initiate photocatalytic reaction. UV-vis DRS and PL spectra were applied to evaluate the light harvesting and charge separation for HELH, HEO-Cl, and HEO-F, respectively (Figure 2e,f). As displayed in Figure 2e, HELH exhibits a broad and strong absorption band in 200–1000 nm range, consisting of three distinct overlapping and gradually attenuated peaks at ≈400, 500, and 700 nm, which are ascribed to ligand-to-metal charge transfer ($O^{2-} \rightarrow M^{2+}$), metal-to-metal charge transfer (MMCT) and low-spin M^{3+} absorption in an octahedral geometry, respectively.[38,39] Compared to HELH, both HEO-Cl and HEO-F show almost no change in the first peak (400 nm), suggesting that the NH_3 complexation has negligible interference with the charge transfer between the ligand and metal ($O^{2-} \rightarrow M^{2+}$). For the peaks centered at 500 and 700 nm across visible and near-IR ranges, negligible change is observed in HEO-Cl, while HEO-F shows relatively weaker absorption, particularly in the near-infrared region. This contrast indicates that the NH_3 complexation with Cl^- modulation has a negligible effect on the metal-to-metal charge transfer (MMCT) and low-spin M^{3+} absorption, whereas the F^- modulation strongly suppresses both phenomena by inducing stronger complexation of Co, Ni, and Cu,[23] as is consistent with the ICP and EDS results. Nevertheless, the broad energy distribution enabling photocatalysis in HEO-F (200–800 nm) aligns with both simulated xenon light and real sunlight spectra (Figure S17, Supporting Information), exhibiting absorption intensity superior to most reported semiconductor photocatalysts.[40,41] Such excellent full-spectrum solar absorption is essential for maximizing solar utilization by driving photothermal conversion (kinetics enhancement) and boosting carrier generation. Under 1400-mW cm^{-2} light, the local catalyst surface temperature of HEO-F detected by infrared thermography rapidly increases from ≈35 to 160 °C upon illumination, stabilizes negligibly decaying over 120 min, then drops immediately to ≈35 °C after the light is turned off (Figure S18, Supporting Information). This confirms that the HEO-F has exceptional photothermal conversion capabilities, superior to that of HELH (150 °C) and binary hydroxide (e.g., CoAl-LDH (65 °C)),[42] demonstrating the effectiveness of high-entropy engineering in enhancing photothermal conversion.

In addition to promoting carrier generation, photocatalytic performance also depends on efficient charge separation. To investigate this, PL spectra reveal a broad and distinct emission band centered at 420 nm (320–480 nm) for all three samples, attributed with charge carrier recombination[43] (Figure 2f). HEO-Cl exhibits slightly lower PL intensity than HELH, while HEO-F shows dramatically attenuated signals. This phenomenon indicates that the change separation efficiency follows the order: HELH < HEO-Cl < HEO-F, confirming that suppressed electron-hole recombination is presented in both NH_3-complexed samples relative to HELH. Notably, the synergistic modulation with F^- anion further enhances the photoinduced charges separation and transfer in HEO-F, resulting in the greatest PL quenching, thereby boosting the further generation of free radicals. Thus, although F^- modulation slightly reduce visible-to-NIR light absorption, it retains functional superiority in achieving the highest charge separation efficiency.

The generation of reactive oxygen species including superoxide and hydroxyl radicals ($\bullet O_2^-$ and •OH) for HELH, HEO-Cl, and HEO-F was monitored by electron spin resonance (ESR) spectroscopy using 5,5 dimethyl-1-pyrroline N-oxide (DMPO) as the spin trap. Figure 2g shows that a typical six-fold peak attributed to DMPO-$\bullet O_2^-$ adducts emerges after 10 min of light irradiation, with signal intensities following the order: HELH < HEO-F < HEO-Cl. This result suggests that NH_3 complexation is beneficial for promoting the generation of $\bullet O_2^-$, particularly under Cl^- modulation. Notably, this trend contradicts the charge separation efficiency, suggesting that the formation of $\bullet O_2^-$ is not only controlled by the electron supply, but also involves other factors, especially the adsorption of oxygen (quantified in the subsequent section).

In addition, DMPO-•OH signals were also recorded and the results are shown in Figure 2h. All samples exhibit characteristic quadruple DMPO-•OH peaks under dark conditions. Notably, the intensity of dark-generated •OH radicals over HEO-F significantly surpasses that of HEO-Cl and HELH. After 10 min of light irradiation, only a slight intensity increase is observed in HEO-F, while negligible changes are shown in HEO-Cl and HELH as compared with dark conditions. These trends are well consistent with the increased trend of OV concentration before and after irradiation (Figure 2i), indicating that a substantial portion of •OH generation in HEO-F, HEO-Cl and HELH is independent of light excitation, originating likely from the activation of O_2 and H_2O (or -OH) by the abundant OV sites. Combined DMPO-$\bullet O_2^-$ and DMPO-•OH results indicate that NH_3 complexation effectively promotes the generation of $\bullet O_2^-$ and •OH. Interestingly, although HEO-F exhibits superior •OH generation, its production of photo-induced $\bullet O_2^-$ is dramatically lower than that of HEO-Cl. This inverse correlation suggests that the F^- modulation alters the primary reactive oxygen species generation pathway, favoring the direct formation of •OH even in the absence of light, which is a distinct advantage for sustained adsorption activation-catalytic oxidation reactions.

2.3. Simulation Calculations of Reactant Adsorption and Activation from Atomic Scale

Efficient reactant adsorption and activation are crucial prerequisites for initiating photothermal catalysis. To elucidate the atomic-scale mechanisms, DFT calculations were performed to determine adsorption energies (E_{ads}) and charge density differences (Δq) of oxygen (O_2), hydroxyl (OH) and toluene (C_7H_8) on HEO-F surface. As shown in **Figure 3a–c**, the E_{ads} values for O_2, OH, and C_7H_8 on HEO-F are −1.99, −4.07, and −1.11 eV, respectively. These results indicate that the HEO-F exhibit stronger adsorption toward O_2 and OH compared to C_7H_8, which is beneficial for facilitating the preferential activation of O_2 and OH for the formation of $\bullet O_2^-$ and •OH. Additionally, the Δq results show that the electron transfer amounts for O_2 (−0.82 e) and OH (−0.76 e) on HEO-F are significantly greater than those for C_7H_8

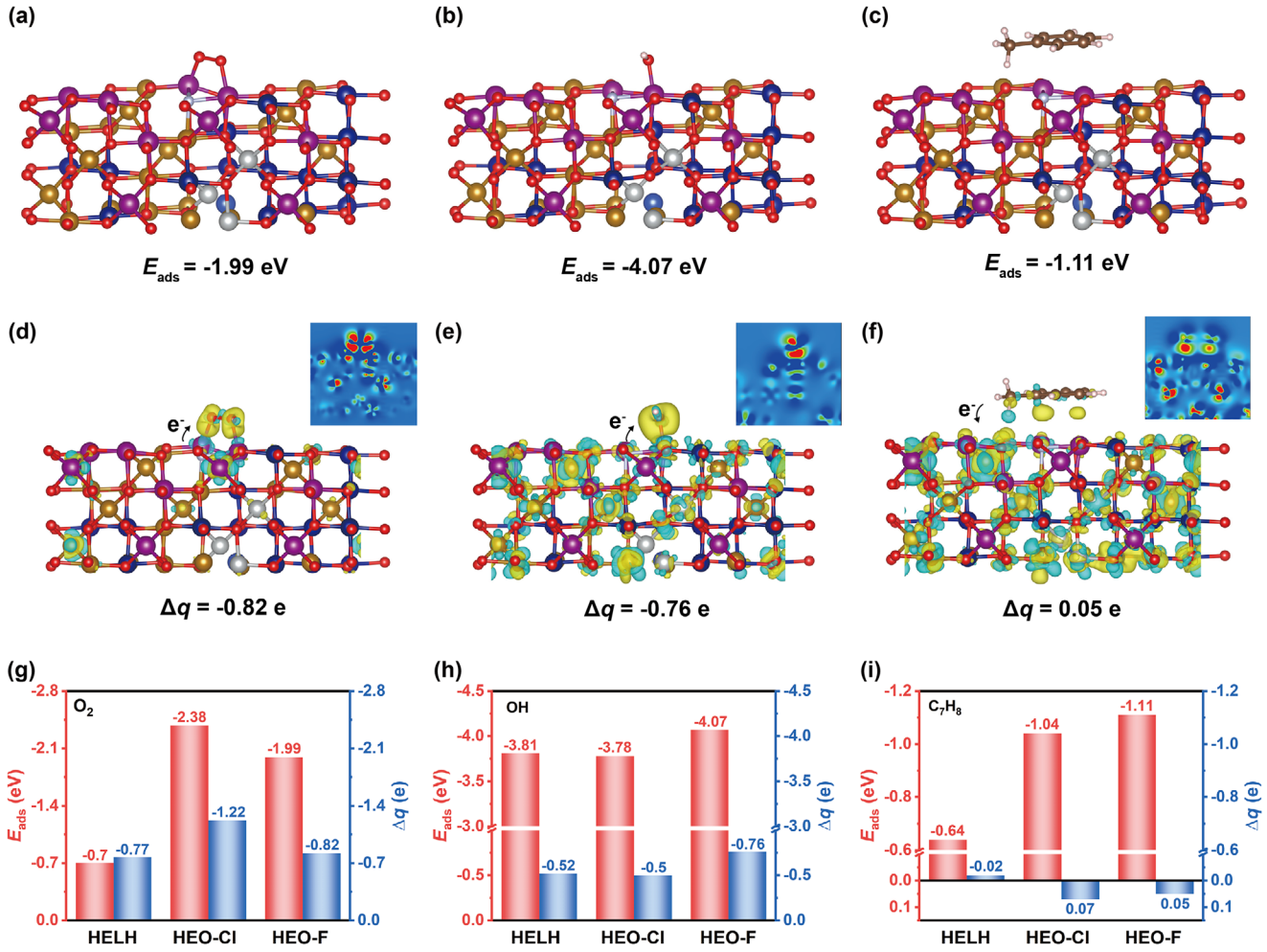

Figure 3. a) O_2, b) OH, and c) C_7H_8 adsorption simulation of HEO-F; Charge density differences of d) O_2, e) OH, and f) C_7H_8 on HEO-F; Adsorption energies and charge density differences of g) O_2, h) OH, and i) C_7H_8 on HELH, HEO-Cl, and HEO-F.

(0.05 e) (Figure 3d–f). Therefore, O_2 and OH are more likely to be first activated on the catalyst surface, promoting the ROS generation, which is critical for the subsequent activation of adsorbed toluene.

The E_{ads} and Δq values of O_2, OH, and C_7H_8 over HELH and HEO-Cl were also calculated and compared with those of HEO-F, and the results are shown in Figures S19, S20 (Supporting Information), and Figure 3g–i, respectively. As displayed in Figure 3g, HEO-Cl exhibits the strongest O_2 adsorption energy (−2.38 eV), much higher than HEO-F (−1.99 eV) and HELH (−0.7 eV). A consistent change order is observed in the Δq values of O_2: HEO-Cl (−1.22 e) > HEO-F (−0.82 e) > HELH (−0.77 e), where negative Δq represents that the electron is transferred from the catalyst to O_2.[44] Figure 3h shows that the E_{ads} value for OH on HEO-F (−4.07 eV) is obviously greater than that of HEO-Cl (−3.78 eV) and HELH (−3.81 eV). HEO-F also exhibits a stronger Δq (0.76 e) for O_2 adsorption than HEO-Cl (0.5 e) and HELH (0.52 e), with positive sign suggesting electron donation from the catalyst to OH.[45] These increased trends have good agreement with those observed in the DMPO-•O_2^- and DMPO-•OH signals, confirming that the enhanced adsorption and activation of O_2 and OH are highly responsible for boosting the formation of •O_2^- and •OH radicals.

As shown in Figure 3i, the E_{ads} values of C_7H_8 follow the order: HEO-F (−1.11 eV) > HEO-Cl (−1.04 eV) > HELH (−0.64 eV), indicating that HEO-F and HEO-Cl exhibit superior adsorption energy. This is possibly due to the enhanced Lewis acidity and stronger toluene-catalyst interaction, as evidenced by the Py-IR and toluene-TPD results. Furthermore, the Δq results for C_7H_8 on the catalysts further reveal that the HEO-F (0.07 e) and HEO-Cl (0.05 e) exhibit similar electron transfer amounts, which are significantly higher than HELH (−0.02 e). Notably, the direction of electron transfer also varies from the catalysts due to the different sign of Δq. For HEO-F and HEO-Cl, a positive Δq value means a net electron transfer from C_7H_8 to the catalysts, while for HELH, the electron transfer direction is reversed (from the catalyst to C_7H_8). This phenomenon can be attributed to the significantly higher Lewis acid content in HEO-F and HEO-Cl, where Lewis acid sites (electron acceptors) interact with Lewis-basic C_7H_8 (electron donors). Thus, HEO-F and HEO-Cl demonstrate great potential for enhancing toluene adsorption and activation.

2.4. Photothermal Catalytic Performance Toward Toluene Conversion

Photothermal catalytic performance of HELH, HEO-Cl and HEO-F was evaluated by mineralization of gaseous toluene in a continuous flow system. To distinguish the photothermal catalytic activity, an adsorption-desorption equilibrium was established for all catalysts prior to light irradiation. As shown in **Figure** 4a, the adsorption efficiency of HELH gradually rises to ≈40% within 30 min time on stream (TOS), then slowly declines to ≈20% with time increasing to ≈110 min. In contrast, HEO-Cl exhibits a rapid increase to 60% of adsorption efficiency within 5 min, followed by a continuous rise to a maximum up to 90% at 80 min, then undergoes a sharp decline to 20% at ≈140 min. Compared to HEO-Cl, a much faster and higher adsorption is observed in HEO-F, with the efficiency sharply rising to 90% within 5 min, further increasing to ≈100% within 30 min, and then maintaining a saturation plateau until 60 min. Subsequently, HEO-F exhibits a decline trend similar to HEO-Cl from the maximum (≈100%) to minimum (<20%). These results demonstrate that HEO-F displays the fastest kinetics and highest adsorption efficiency, followed by HEO-Cl, both substantially outperforming HELH, which is consistent with the increased trend as observed in the results of toluene adsorption energy. The analogous superior adsorption behavior of HEO-F and HEO-Cl is attributed their optimized adsorption properties (increased S_{BET}, enlarged pore volume and enhanced Lewis acidity), confirming the advantage of the synergy of NH_3 complexation and halogen modulation for toluene adsorption.

Following the toluene adsorption-desorption equilibrium, the photothermal catalytic activity of the three catalysts for toluene conversion under simulated solar irradiation coupled with mild external heating (light+90 °C) was investigated, and the results are shown in Figure 4b. For all catalysts, a pronounced negative peak corresponding to toluene desorption emerged within the initial 5 min. This phenomenon arises from the rapid photothermal heating induced desorption, a characteristic behavior in continuous-flow systems for catalysts with high equilibrium adsorption capacities.[46] As the reaction prolongs, HELH exhibits a gradual increase in toluene conversion, reaching a maximum of ≈90% at 35-min TOS. Subsequently, it suffers from obvious deactivation, gradually declining to 65% after 180 min, which may be due to carbonaceous intermediate accumulation blocking active sites. In contrast, HEO-Cl displays rapid photothermal activation, achieving 90% toluene conversion within 15 min. However, slight deactivation occurs after reaching its maximum conversion (96%) at 30 min, dropping to 90% after 180 min. Notably, HEO-F sharply rises to 100% in toluene conversion within 30 min, with negligible deactivation over 180 min. Among them, HEO-F exhibits the best catalytic performance in terms of kinetics, toluene conversion, especially stability. Although HEO-F and HEO-Cl demonstrate comparable initial toluene conversion under photothermal conditions, their stability profiles diverge markedly after prolonged reaction. This divergence in stability could be attributed to the distinct reactive oxygen species generation as revealed by ESR. We propose that the high activity of HEO-Cl is primarily driven by photo-dependent $\bullet O_2^-$, which is potent but susceptible to deactivation possibly due to the intermediate species that accumulate and block active sites. In contrast, the performance of HEO-F is well maintained by its superior capacity for light-independent •OH generation, where the redox potential of •OH is significantly higher than that of $\bullet O_2^-$.[47] This sustained supply of •OH enables pre-activation of toluene prior to irradiation, which is crucial for initiating the radical chain reaction that achieves toluene ring-opening and mineralization. Thus, HEO-F with excellent activity and stability is selected as the optimal catalyst for further toluene conversion optimization.

In order to elucidate the correlation between the enhanced photothermal catalysis of HEO-F and the increased dark •OH radicals, the radical generation and trapping control experiments were conducted, and the results are shown in Figure S21 (Supporting Information). Thereinto, dry air, humid air and humid air with tert-butanol (humid air + TBA) were served as •OH-suppressed, •OH-enabled, and •OH-scavenged conditions, respectively.[48] Compared to the benchmark humid air condition, the obvious suppression in both the dark adsorption and the subsequent photothermal catalytic stability is presented under both "dry air" and "humid air + TBA", which directly confirm that the dark •OH radicals are critically involved from the very beginning of the adsorption process. Their presence during the initial dark stage initiated the oxidative adsorption of toluene, which subsequently contributed to maintaining catalytic stability in the following photothermal stage.

To further determine the optimal light intensity and heating temperature, the toluene conversion of HEO-F was evaluated in under varying intensities and temperatures. Under sole light irradiation, as displayed in Figure S22 (Supporting Information), although the maximum toluene conversion at 600 mW cm^{-2} is close to that at 1000 mW cm^{-2}, the stability is obviously improved with increasing intensity. Notably, the kinetics and maximum in toluene conversion significantly increases as the intensity rises from 1000 to 1400 mW cm^{-2} over 60 min, resulting in the high and stable toluene conversion (up to ≈100%). Figure S23 (Supporting Information) shows that increasing the heating temperature from 60 to 90 °C reduces the time required to reach the maximum value from 70 to 40 min, resulting in a clearly higher peak (≈20%), but it then gradually declines to a value similar to the former (≈10%) from 70 to 120 min. Further increasing the temperature to 120 °C enables the initial conversion to reach 40% at 50 min, but it then slowly decreases to ≈30% at 120 min. These results demonstrate that increasing light intensity improves photothermal toluene conversion on HEO-F more effectively than raising temperature. Balancing the availability of concentrated solar energy with the need to reduce non-renewable thermal energy consumption, the optimal conditions are determined to be 1400 mW cm^{-2} and 90 °C. Under the optimal conditions, HEO-F achieves complete toluene conversion (100%) with negligible deactivation over 180 min, significantly higher than mechanically mixed oxides (<20%), confirming the effective high-entropy engineering (Figure 4c). In addition to the high toluene conversion (η), the long duration (η <20%) and complete CO_2 selectivity (100%) demonstrate the superior photothermal catalytic performance of HEO-F, which is striking when comparing to most of the state-of-the-art Mn- and Co-based oxide catalysts (Figure 4d; Table S7, Supporting Information). Notably, the HEO-F maintains 100% toluene conversion for over 300 min-TOS, with only marginal decay (≈4%) observed after >660 min

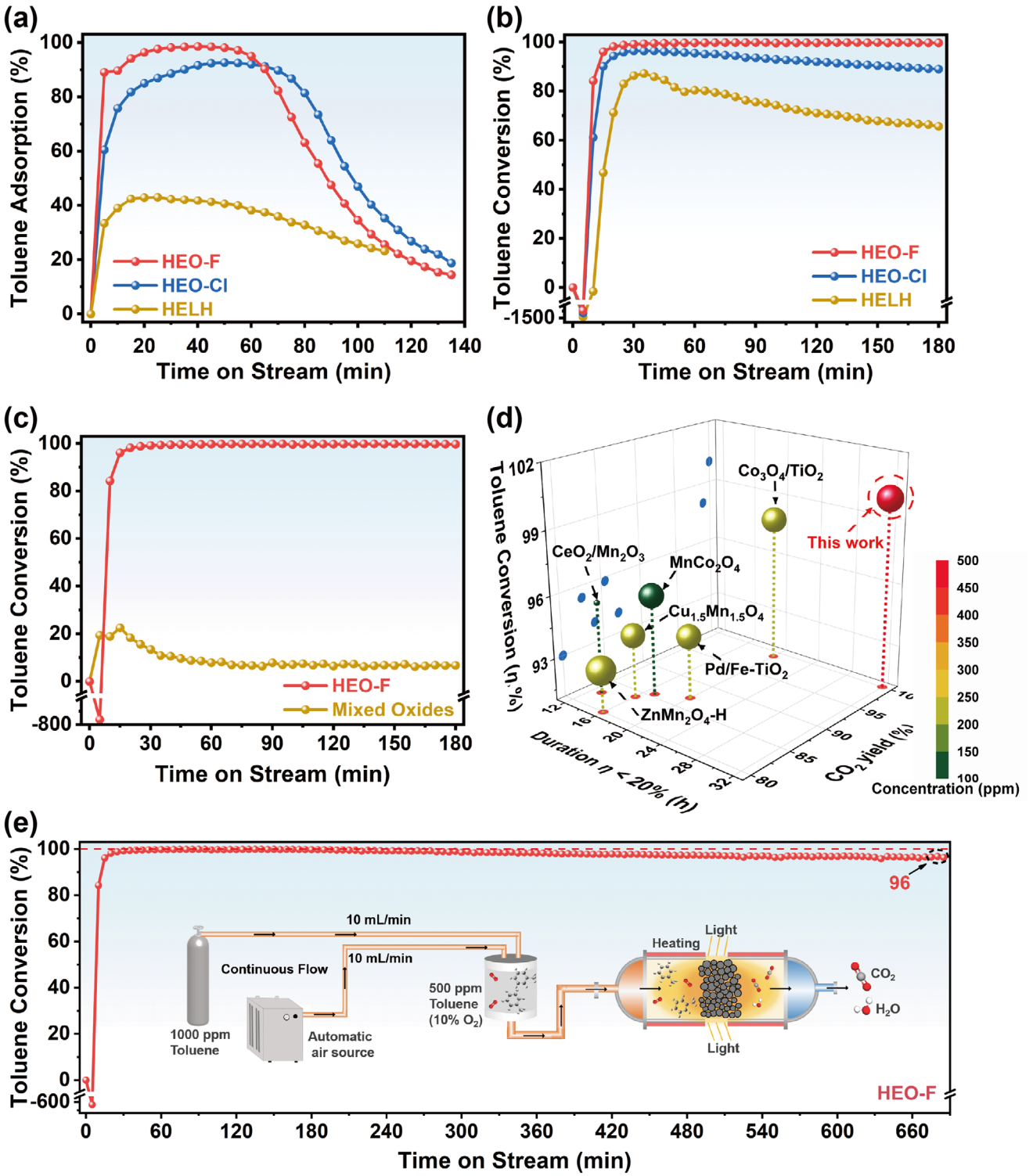

Figure 4. a) Toluene adsorption and b) photothermal catalytic conversion of toluene over HELH, HEO-Cl, and HEO-F; c) Photothermal catalytic performance of HEO-F and mixed oxides for toluene conversion; d) Comparison of HEO-F and various photothermal catalysts in toluene oxidation under photothermal conditions; e) Long-term photothermal catalytic conversion of toluene in HEO-F.

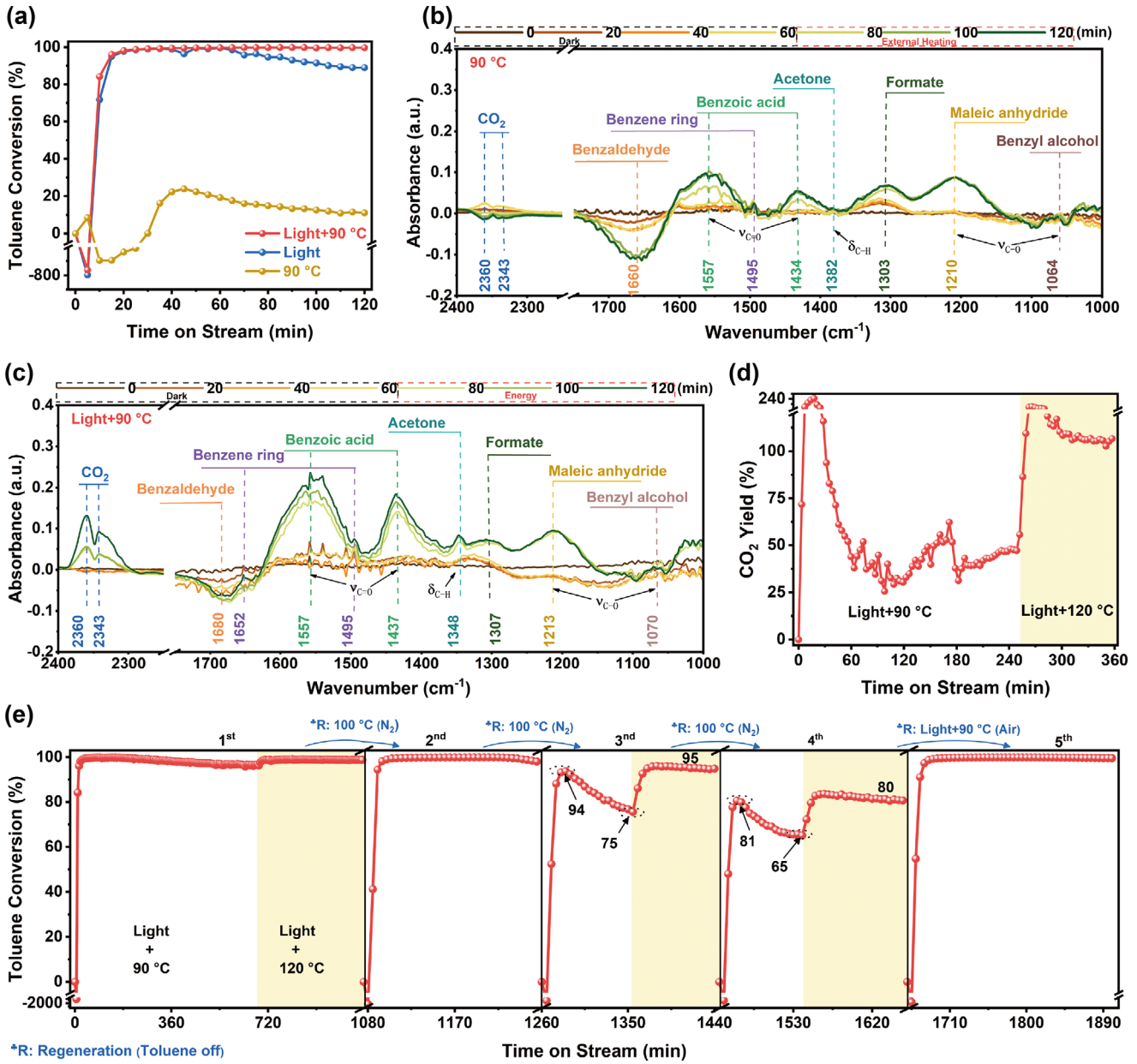

Figure 5. a) Comparison of toluene conversion of HEO-F under varying conditions; In situ DRIFT spectra of toluene over HEO-F during b) thermal reaction at 90 °C and c) photothermal reaction at 90 °C with 1400 mW cm^{-2} irradiation, monitored through dark adsorption (0–60 min) and catalytic reaction (60–120 min) phases; d) CO_2 yield of HEO-F; e) Long-term cycling activity and stability of photothermal catalytic toluene conversion over HEO-F.

(Figure 4e). These results demonstrate that HEO-F exhibits outstanding activity, 100% selectivity and exceptional long-term stability for photothermal catalytic toluene conversion.

2.5. Enhancement Mechanism and Intermediate Dynamics During Photothermal Catalysis

To decouple photothermal contributions, the toluene conversion of HEO-F was evaluated under three modes: "90 °C", "light" and "light+90 °C". **Figure** 5a shows that the "light+90 °C" mode maintains a stable 100% conversion for up to 120 min, significantly outperforming the "90 °C" and "light" modes, which exhibits very low conversion efficiency (20% for "90 °C") and a gradual declined activity (a total loss of ≈10% over 120 min for "light"). These results indicate that the light irradiation is crucial for achieving the maximum activity, while mild heating sustains highly stable toluene conversion. During the reaction processes, Figure S24 (Supporting Information) shows that the near-bed gas temperature in "light+90 °C" mode (≈110 °C) exceeds the heating temperature (90 °C) due to photothermal self-heating of HEO-F. To further quantify the photocatalysis

and thermal catalysis contributions, we compared the conversion under "light+90 °C" with that under pure thermal catalysis at the temperature ≈110 °C. Based on the positive temperature-conversion relationship (Figure S23, Supporting Information) that pure thermal catalysis at 90–120 °C results in 20–40% conversion, it can be inferred that the maximum thermal contribution at ≈110 °C is ≤40%, implying that photocatalysis contributes to >60%. This confirms the photothermal catalysis synergy that photocatalysis is dominant in reaching high activity, while the thermal catalysis accelerated kinetics and stability.

To gain deeper insights into the molecular mechanisms and intermediate dynamics governing the photothermal catalysis synergy, in situ DRIFTS were employed on HEO-F under there modes: "90 °C", "light" and "light+90 °C" (Figure 5b,c, Figure S25, Supporting Information). Prior to the energy (light or heat) input period, several week peaks of intermediates are identified after stabilizing toluene/air flow for 20 min, which remained stable for 60 min. These intermediates are including toluene (≈1495 and 1647–1652 cm^{-1}), benzyl alcohol (1035–1070 cm^{-1}), benzaldehyde (1689 cm^{-1}; negative peak meaning consumption), benzoic acid (1434 and 1557 cm^{-1}), and formate (1303–1316 cm^{-1}).[46,49–51] This observation provides direct molecular-level evidence for the pre-activation of toluene, which is consistent with the enhanced dark adsorption capacity, revealing spontaneous surface reactions initiated by dark-generated •OH radicals. During the energy input period, Figure S25 (Supporting Information), Figure 5b,c demonstrate consistent toluene oxidation pathways on HEO-F across all modes, evidenced by identical spectral peak positions, except for varying in intensities. The reaction follows the benzyl alcohol pathway: toluene → benzyl alcohol → benzaldehyde → benzoic acid → maleic anhydride → formate → CO_2.[51] Temporal evolution of these species (Figure S26, Supporting Information) shows the orders: benzaldehyde (90 °C > light ≈ light+90 °C), benzoic acid (light+90 °C > 90 °C > light), maleic anhydride (light+90 °C > 90 °C > light), respectively. These trends reveal that: (1) Mild heat preferentially promotes initial C—H bond cleavage of toluene, leading to the highest yield of benzaldehyde at 90 °C; (2) light irradiation readily oxidizes benzaldehyde to benzoic acid; however, its efficiency in subsequent ring-opening steps is limited, as evidenced by the accumulation of benzoic acid under light alone. (3) Combined light and heat energy are critical for enhancing the deep oxidation and complete mineralization of toluene, as verified by the "light+90 °C" mode that the promoted benzoic acid conversion to maleic anhydride and CO_2. Combined toluene conversion and in situ DRIFTS results reveal a photothermal synergistic mechanism that thermal catalysis accelerates kinetics and stability by preferentially initiating the reaction (C—H cleavage), while photocatalysis dominants in reaching high activity through driving intermediate oxidation. However, it is their combined action that effectively overcomes the critical bottleneck of the ring-opening of benzoic acid for obtaining both high activity and stability.

In addition, it is observed that the highest CO_2 product signal of HEO-F under "light+90 °C" mode in Figure 5c significantly exceeds that under the "90 °C" mode (Figure 5b), indicating the photothermal catalytic synergy also facilitates deep oxidation and complete mineralization of toluene, thereby sustaining highly efficient toluene conversion. In contrast, HELH shows negligible CO_2 signal and obvious carbon accumulation (Figure S27, Supporting Information), accompanied by the absent of benzoic acid peaks (Figure S27, Supporting Information). This observation suggests that the HELH favored the graphitization pathway over the ring-opening of benzoic acid, resulting in carbon accumulation.[52,53] These results demonstrate that HEO-F exhibits superior toluene mineralization performance over HELH, originating from its higher OVs content, which enabled more abundant dark •OH generation and greater lattice oxygen mobility.

Stability and regeneration ability of HEO-F were further evaluated over long-term tests and multiple cycles (Figure 5d,e). As shown in Figure 5d, the CO_2 yield rapidly declines to an average steady state below 50% under "light+90 °C", which is probably due to the blocked active sites by accumulation species. After the heating temperature is increased to 120 °C, the CO_2 yield is rapidly and completely restores and maintains stable at 100%. This demonstrating the thermal energy effectively regenerates active sites by facilitating desorption or lattice oxygen activation. Figure 5e displays that that HEO-F in the long-term cyclic tests (31.5 h) could be completely regenerated under photothermal oxidative conditions ("light+90 °C", air) for recovering 100% conversion, whereas inert calcination only enables it temporary recovery. This demonstrates the self-regenerating capability of HEO-F under aerobic photothermal conditions. XRD patterns of HEO-F after post-reaction at 4th and 5th cycles in the above long-term cyclic tests confirm well retained oxygen phase and crystal structure (Figure S28, Supporting Information), demonstrating the structural robustness and practical potential of the HEO-F in photothermal catalysis.

Based on the above observations, a possible photothermal catalytic toluene oxidation reaction pathway on the surface of HEO-F was proposed (**Figure 6**). First, prior to the energy (light or heat) input, the gaseous toluene molecules are rapidly adsorbed into the developed pore structure, which is partially oxidized by the dark-generated •OH radicals. Then, the photothermal synergy driven by the combined input of simulated sunlight and mild heat (≈90–120 °C) readily overcome the ring-opening barrier, leading to the highest conversion of benzoic acid to maleic anhydride, and promoting the production and desorption CO_2. This follows the benzyl alcohol pathway: toluene → benzyl alcohol → benzaldehyde → benzoic acid → maleic anhydride → formate → CO_2. During the synergistic photothermal catalysis, the mild heat energy primarily promotes the initial C-H bond cleavage of toluene and accelerates the formation of benzaldehyde. Meanwhile, the light irradiation effectively facilitates the conversion of benzaldehyde to benzoic acid. Only through the combined heat and light energy can the ring-opening reaction of benzoic acid be effectively promoted, thereby accelerating the subsequent mineralization pathways. The ring opening of benzoic acid is a key step to prevent the HEO-F from carbon deposition and rapid deactivation, which is greatly reliant on the photothermal synergistic effect, and the abundant OVs, O_{latt} and •OH species. Consequently, the effective integration of dark •OH enhanced oxidation and synergistic photothermal catalysis enables HEO-F to achieve substantial advancements across the entire reaction steps, leading to the highly efficient and durable photothermal catalytic performance.

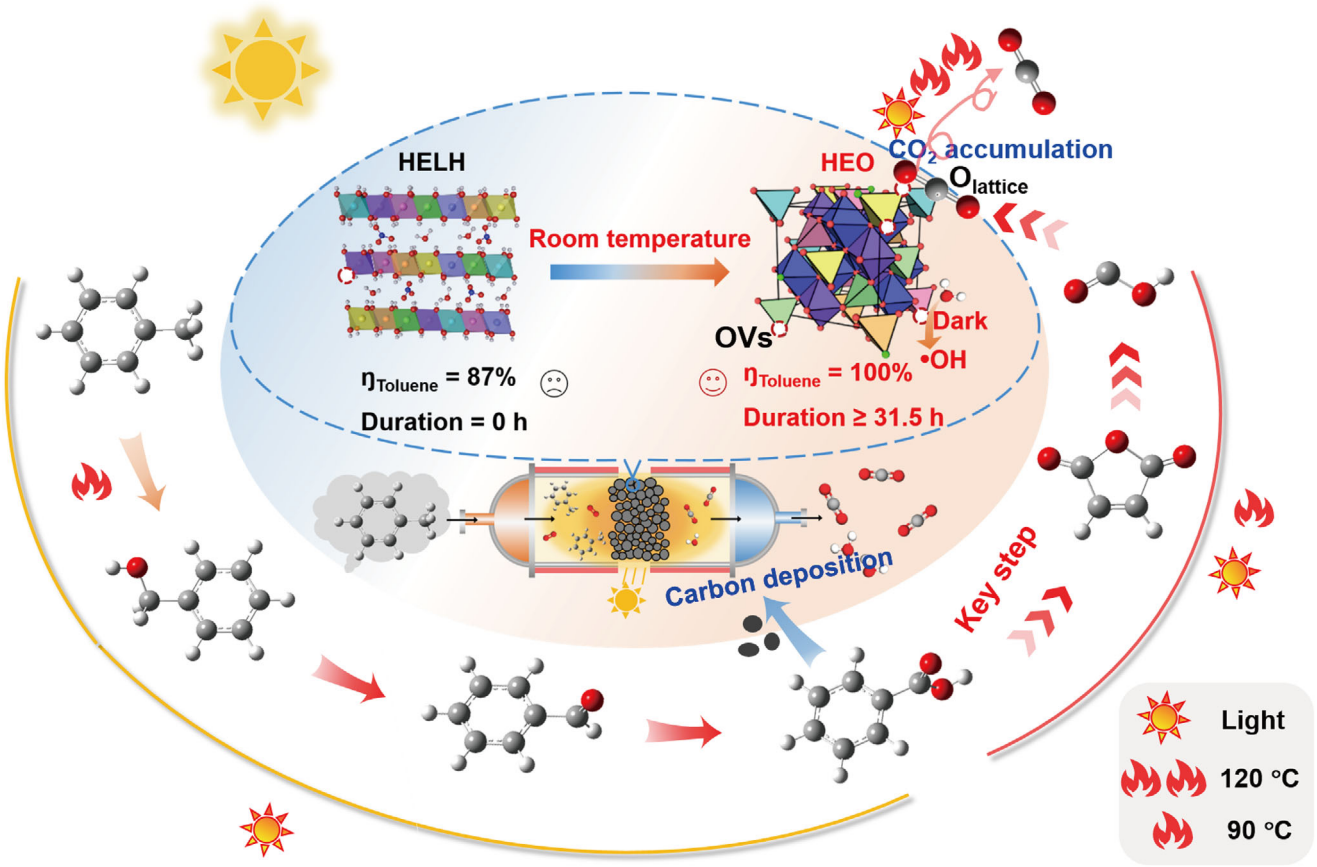

Figure 6. Schematic of synergistic photothermal catalytic mechanism for toluene conversion.

3. Conclusion

In summary, we propose an NH_4F-modulated competitive complexation precipitation strategy for room-temperature synthesis of HEO-F. This strategy involves mixing NH_4F complexing modulators with multiple 3d metal (Cr, Mn, Fe, Co, Ni, and Cu) ions under alkaline conditions. By modulating the NH_4^+/OH^- ratio and multiple A-site metal ions, the complexation precipitation equilibrium direction is adjustable, enabling a controllable phase transformation from hydrotalcite to oxide at room temperature. NH_3 complexation and F^- modulation synergistically drive the OVs formation, significantly enhancing adsorption and activation toward O_2, OH, and toluene, as confirmed by ROS measurements, TPD tests, and DFT calculations. Notably, the F^- incorporation significantly promotes the dark generation of •OH radicals without any external energy input.

The resulting HEO-F exhibits superior photothermal catalytic performance, achieving 100% toluene conversion for >300 min with 100% CO_2 selectivity under mild conditions ("light+120 °C"), outperforming counterparts (HELH and HEO-Cl) and most of previously reported Mn/Co-based catalysts. Control experiments of radical generation and trapping confirm the key role of dark •OH radical in the enhanced adsorption and long-term stability in photothermal catalysis. In situ DRIFT spectra reveal that the adsorption oxidation and the synergistic photothermal catalysis collectively drive HEO-F to overcome the ring-opening barrier, leading to maximized benzoic acid conversion to maleic anhydride and ultimately CO_2. Long-term cyclic tests demonstrate the excellent regeneration ability of HEO-F after >30 h of continuous operation. This work not only demonstrates a facile, low-cost, and green route for room-temperature fabrication of HEO, but also highlights the unique role of engineering dark-generated •OH radicals for highly efficient and stable photothermal catalysis.

Supporting Information

Supporting Information is available from the Wiley Online Library or from the author.

Acknowledgements

This research was financially supported by Natural Science Foundation of Guangxi (No. 2025GXNSFAA069779), National Natural Science Foundation of China (No. 52462027), Opening Project of Guangxi Key Laboratory of Petrochemical Resource Processing and Process Intensification Technology Scientific Research Foundation of Guangxi University (No. 2024K007), and Special Fund for Science and Technology Development of Guangxi (No. AD25069078).

Conflict of Interest

The authors declare no conflict of interest.

Data Availability Statement

The data that support the findings of this study are available from the corresponding author upon reasonable request.

Keywords

anti-deactivation, hydroxyl radical, MnCo-based oxide, toluene oxidation

Received: September 30, 2025
Revised: December 5, 2025
Published online: December 13, 2025

[1] C. He, J. Cheng, X. Zhang, M. Douthwaite, S. Pattisson, Z. Hao, *Chem. Rev.* **2019**, *119*, 4471.
[2] Y. Miao, Y. Zhao, G. I. N. Waterhouse, R. Shi, L.-Z. Wu, T. Zhang, *Nat. Commun.* **2023**, *14*, 4242.
[3] C. Feng, F. Raziq, H. Huang, Z.-P. Wu, H. S. Aqahtani, R. Alqahtani, M. Z. Rahman, B. Chang, J. Gascon, H. Zhang, *Adv. Mater.* **2025**, *37*, 2410387.
[4] A. J. Martin, S. Mitchell, C. Mondelli, S. Jaydev, J. Perez-Ramirez, *Nat. Catal.* **2022**, *5*, 854.
[5] J. Xu, K. Gu, P. Wang, P. Cheng, H. Che, C. Tang, K. Zhang, Y. Ao, *Nat. Commun.* **2025**, *16*, 7908.
[6] X. Liu, H. Ma, M. Zhang, P. Che, Y. Luo, S. Zhang, J. Xu, *ACS Catal.* **2023**, *13*, 11104.
[7] M. Zhang, G. Li, Q. Li, J. Chen, E. A. Elimian, H. Jia, H. He, *Environ. Sci. Technol.* **2023**, *57*, 4286.
[8] Z. Su, X. Li, W. Si, L. Artiglia, Y. Peng, J. Chen, H. Wang, D. Chen, J. Li, *ACS Catal.* **2023**, *13*, 3444.
[9] Y. Zheng, K. Fu, Z. Yu, Y. Su, R. Han, Q. Liu, *J. Mater. Chem. A* **2022**, *10*, 14171.
[10] M. Zhang, X. Duan, Y. Gao, S. Zhang, X. Lu, K. Luo, J. Ye, X. Wang, Q. Niu, P. Zhang, S. Dai, *ACS Appl. Mater. Interfaces* **2023**, *15*, 45774.
[11] M. Rafique, T. Yao, S. Ma, Y. Xu, L. Li, J. Han, Q. Fu, W. Li, Z. Yuan, K. Wang, B. Song, *Adv. Funct. Mater.* **2025**, 12495.
[12] C.-Y. He, Y. Li, Z.-H. Zhou, B.-H. Liu, X.-H. Gao, *Adv. Mater.* **2024**, *36*, 2400920.
[13] C. M. Rost, E. Sachet, T. Borman, A. Moballegh, E. C. Dickey, D. Hou, J. L. Jones, S. Curtarolo, J.-P. Maria, *Nat. Commun.* **2015**, *6*, 8485.
[14] D. Chen, S. Nie, L. Wu, X. Zheng, S. Du, X. Duan, Q. Niu, P. Zhang, S. Dai, *Chem. Mater.* **2022**, *34*, 1746.
[15] J. Zander, J. P. Woelfel, M. Weiss, Y. Jiang, N. Cheng, S. Zhang, R. Marschall, *Adv. Funct. Mater.* **2024**, *34*, 2310179.
[16] L. Zhang, S. Xia, X. Zhang, Y. Yao, Y. Zhang, S. Chen, Y. Chen, J. Yan, *ACS Nano* **2024**, *18*, 5322.
[17] L. He, H. Kang, G. Hou, X. Qiao, X. Jia, W. Qin, X. Wu, *Chem. Eng. J.* **2023**, *460*, 141675.
[18] Z. Luo, X.-P. Zhou, *Sci. Adv.* **2025**, *11*, adw1461.
[19] L. Spiridigliozzi, M. Bortolotti, V. Monfreda, G. Dell'Agli, *J. Alloys Compd.* **2025**, *1040*, 183683.
[20] K. M. Siniard, M. Li, Y. Cai, J. Zhang, F. Polo-Garzon, D. M. Driscoll, A. S. Ivanov, X. Lu, H. Chen, Y. Li, Z. Wu, Z. Yang, S. Dai, *ACS Catal.* **2024**, *14*, 14807.
[21] Y. Shen, H. Xue, S. Wang, D. Zhang, D. Yin, L. Wang, Y. Cheng, *Chem. Eng. J.* **2021**, *411*, 128487.
[22] W. Guo, C. Dun, M. A. Marcus, V. Venturi, Z. Gainsforth, F. Yang, X. Feng, V. Viswanathan, J. J. Urban, C. Yu, Q. Zhang, J. Guo, J. Qiu, *Adv. Mater.* **2023**, *35*, 2211603.
[23] H. Li, in *Coordination Chemistry*, Chemistry Industry Press Co., Ltd, Beijing, China **2025**, https://www.cip.com.cn/Book/Index/45837.
[24] Q. Chen, Y.-H. Chen, J.-R. Zhu, Z.-Y. Li, F.-X. Xiao, *Adv. Funct. Mater.* **2025**, *35*, 2417139.
[25] L. Yan, Y. Han, C. Zhu, L. Luo, Y. Qin, D. Yu, B. Liu, X. Zou, Y. Zhou, B. Xiang, *Nano Energy* **2024**, *122*, 109331.
[26] C.-W. You, T. Fu, C.-B. Li, X. Song, B. Tang, X. Song, Y. Yang, Z.-P. Deng, Y.-Z. Wang, F. Song, *Adv. Funct. Mater.* **2022**, *32*, 2208131.
[27] Y. Sun, B. Yin, J. Yang, Y. Ding, M. Li, H. Li, J. Li, B. Jia, S. Zhang, T. Ma, *Energy Environ. Sci.* **2023**, *16*, 5568.
[28] P.-H. Chang, W.-T. Jiang, Z. Li, *J. Hazard. Mater.* **2019**, *368*, 487.
[29] T. X. Nguyen, C. C. Tsai, V. T. Nguyen, Y.-J. Huang, Y.-H. Su, S.-Y. Li, R.-K. Xie, Y. J. Lin, J.-F. Lee, J.-M. Ting, *Chem. Eng. J.* **2023**, *466*, 143352.
[30] A. Roy, S. Kumar, A. Guilherme Buzanich, C. Prinz, E. Goetz, A. Retzmann, T. Hickel, B. Bhattacharya, F. Emmerling, *Adv. Mater.* **2024**, *36*, 2408114.
[31] J. Yin, J. Jin, M. Lu, B. Huang, H. Zhang, Y. Peng, P. Xi, C.-H. Yan, *J. Am. Chem. Soc.* **2020**, *142*, 18378.
[32] J. Dantas, E. Leal, A. B. Mapossa, D. R. Cornejo, A. C. F. M. Costa, *Fuel* **2017**, *191*, 463.
[33] B. Hazra, D. A. Wood, V. Vishal, A. K. Varma, D. Sakha, A. K. Singh, *Fuel* **2018**, *220*, 837.
[34] Z. Song, Y. Peng, X. Zhao, H. Liu, C. Gao, W. Si, J. Li, *ACS Catal.* **2022**, *12*, 11505.
[35] D. Yu, L. Xu, K. Fu, X. Liu, S. Wang, M. Wu, W. Lu, C. Lv, J. Luo, *Nat. Commun.* **2024**, *15*, 2241.
[36] S. Wang, M. Zhang, C. Li, L. Xu, W. Jiang, D. Yu, M. Wu, B. Yu, *Sep. Purif. Technol.* **2024**, *330*, 125383.
[37] Y. Guo, M. Wen, S. Song, Q. Liu, G. Li, T. An, *Appl. Catal., B* **2022**, *308*, 121212.
[38] L. Lan, Z. Shi, Q. Zhang, Y. Li, Y. Yang, S. Wu, X. Zhao, *J. Mater. Chem. A* **2018**, *6*, 7194.
[39] M. Zhang, H. Gao, J. Chen, E. A. Elimian, H. Jia, *Appl. Catal., B* **2022**, *307*, 121208.
[40] M. Shi, X. Wu, Y. Zhao, R. Li, C. Li, *J. Am. Chem. Soc.* **2025**, *147*, 3641.
[41] C. Li, H. Xu, H. Xiong, S. Xia, X. Peng, F. Xu, X. Chen, *Adv. Funct. Mater.* **2024**, *34*, 2405539.
[42] R. Bi, Y. Chen, M. Tang, J. Zhu, Y. Zhu, T. Lan, Z. Tong, M. Zhu, *Sep. Purif. Technol.* **2024**, *346*, 127427.
[43] Y. Li, J. Huang, M.-L. Gao, X. Zhang, S. Chen, J.-Y. Liu, H.-L. Jiang, *Angew. Chem., Int. Ed.* **2025**, 202511775.
[44] Y. Chen, S. Ke, X. Yang, L. Shen, M.-Q. Yang, *Adv. Funct. Mater.* **2025**, *35*, 2419519.
[45] J. Kong, S. Song, W. Zhao, Z. Yu, Z. Xiang, G. Li, W. Zhang, T. An, *Appl. Catal., B* **2023**, *339*, 123118.
[46] B. Chen, Y. Duan, J. Tan, Y. Li, S. Li, D. Zhang, *Adv. Funct. Mater.* **2025**, *35*, 2425956.
[47] X. Liu, X. Wang, M. Chu, W. Zhang, J. Fu, S. Li, L. Wang, J. Chen, Q. Zhang, M. Cao, *J. Am. Chem. Soc.* **2025**, *147*, 5228.
[48] Z. Rao, G. Lu, L. Chen, A. Mahmood, G. Shi, Z. Tang, X. Xie, J. Sun, *Chem. Eng. J.* **2022**, *430*, 132766.
[49] G. Gao, Y. Liao, W. Li, Z. Li, H. Xu, W. Huang, N. Yan, L. Fan, Z. Qu, *Chem. Eng. J.* **2022**, *441*, 136127.
[50] Y. Shi, P. Li, H. Chen, Z. Wang, Y. Song, Y. Tang, S. Lin, Z. Yu, L. Wu, J. C. Yu, X. Fu, *Nat. Commun.* **2024**, *15*, 4641.
[51] Z. Wang, S. Xie, Y. Feng, P. Ma, K. Zheng, E. Duan, Y. Liu, H. Dai, J. Deng, *Appl. Catal., B* **2021**, *298*, 120612.
[52] W. Su, P. Xu, T. Ritter, *Angew. Chem., Int. Ed.* **2021**, *60*, 24012.
[53] R. Yu, D. Liu, B. Lou, W. Zhu, S. Guo, X. Gong, Z. Zhang, J. Ye, C. Zhu, *Fuel* **2019**, *247*, 97.